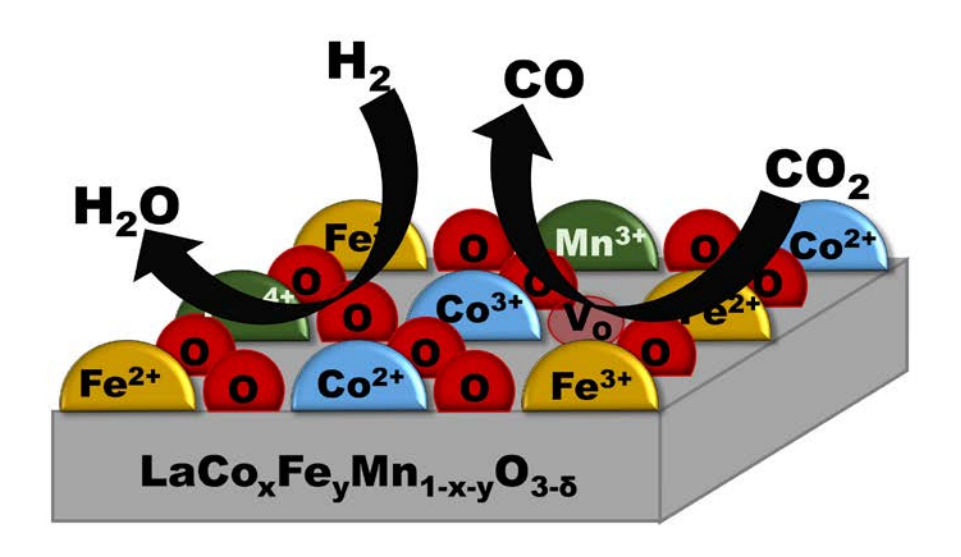
# Co, Fe, and Mn in La-perovskite oxides for low temperature thermochemical CO<sub>2</sub> conversion

Adela E. Ramos, Debtanu Maiti, Yolanda A. Daza, John N. Kuhn\*, Venkat R. Bhethanabotla\*

Department of Chemical & Biomedical Engineering, University of South Florida, Tampa, Florida 33620, United States

\*Email: jnkuhn@usf.edu; bhethana@usf.edu

# **Graphical Abstract**



## **Highlights**

- Low temperature (600°C) CO<sub>2</sub> conversion via reverse water gas shift chemical looping
- Stable operation for several conversion cycles promising for industrial application
- Perovskite oxides with three transition metals in B-site demonstrate CO<sub>2</sub> conversion
- Role of transition metals (Fe, Co, Mn) explored through multiscale approach
- Preferential surface segregation of Co and Fe found favorable for CO<sub>2</sub> conversion

### **Abstract**

Perovskite oxides of the form ABO<sub>3</sub> have shown substantial promise in reverse water gas shift chemical looping (RWGS-CL) process for low temperature thermochemical CO<sub>2</sub> conversion to CO. Transition metals on the 'B' site of these perovskite oxides hold the key to tuning the material properties essential for efficient CO<sub>2</sub> conversion. The role of Co, Fe and Mn in LaBO<sub>3</sub> has been investigated through a combined theoretical and experimental approach. Intrinsic oxygen vacancy formation characteristics of these materials and the electronic charge distribution were explored via ab-initio density functional theory (DFT) simulations, while the microscale properties like crystallite size and CO<sub>2</sub> conversion yield were probed experimentally. Through this multiscale study, the material properties that govern the stable and enhanced CO<sub>2</sub> conversion phenomenon by Fe rich perovskites as opposed to Co and Mn rich phases are differentiated.

<u>Keywords:</u> carbon dioxide conversion; carbon monoxide production; reverse water gas shift chemical looping; RWGS-CL; perovskites.

#### 1. Introduction

Despite \$20 billion in investment [1], Carbon Capture & Storage (CCS) is still an emerging technology, which is limited by technical challenges to lower costs and risks in order to achieve viability. Alternatively, Carbon Capture & Utilization/Use (CCU) is an attractive alternative option due to its closed carbon cycle, but feasibility is currently lacking due to low performance metrics (low CO<sub>2</sub> conversion rates on catalyst amount and/or energy input bases) for various conversion technologies. Due to reliance on fossil fuels and the investments in CCS, a vast amount of CO<sub>2</sub> is or could be available. An estimated 16.67%, 3.73% and 0.28% of total CO<sub>2</sub> emissions, respectively, could be reduced if CO<sub>2</sub> was the sole carbon feedstock for gasoline, methanol, and oil derived chemicals, assuming carbon-free energy sources [2]. However, CO<sub>2</sub> recycling at reasonable scales is limited [3].

Processes transforming CO<sub>2</sub> by first thermochemically converting CO<sub>2</sub> to CO followed by CO hydrogenation to liquid fuels (i.e., methanol, diesel, jet fuel) via Fischer-Tropsch Synthesis (FTS) were found to have higher potential solar energy recovery than technologies involving biomass, algae, or direct photosynthetic conversion of CO<sub>2</sub> to fuel [4]. CO<sub>2</sub> can also be converted by thermochemical, electrochemical, and photochemical approaches. Thermochemical processes include solar thermochemical cycles [5-7], and reverse water gas shift (RWGS) catalytic reaction [2-4], and chemical looping [8-12]. In the RWGS-chemical looping (RWGS-CL) approach, a metal oxide (MO<sub>x</sub>) or mixed metal oxides such as perovskite (ABO<sub>3</sub>) and spinel (AB<sub>2</sub>O<sub>4</sub>) oxides are chemically reduced with hydrogen and subsequently oxidized with CO<sub>2</sub>, producing CO as the material re-oxidizes. As the reduction and oxidation occurs in cycles, this stoichiometric reaction avoids

thermodynamic restraints of the catalytic reaction, provides inherent separation of products, and avoids formation of methane since the carbon and hydrogen species are never fed simultaneously. As a result, the RWGS-CL process is predicted to be more energy efficient than its catalytic counterpart [13]. Since the reduction is thermochemical, as opposed to only thermal in solar thermochemical cycles, operating temperatures of RWGS-CL are lower and range from 400 to 950 °C [8-11], and even isothermal operation has been reported on certain oxides [12, 14]. The selection of materials to balance the reduction by hydrogen, a strong reducing agent, and oxidation by CO<sub>2</sub>, a weak oxidizing agent, is the key in achieving both steps at the same temperature.

Due to their redox properties including non-stoichiometric amounts of oxygen and their ability of accommodating multiple substitutions of A and B site metals simultaneously, perovskite oxides (ABO<sub>3</sub>, where A is a rare earth or alkaline earth metal and B is a transition metal) are ideal material platforms to design new formulations for thermochemical and chemical looping processes. In thermochemical cycles, La<sub>x</sub>Sr<sub>1-x</sub>Mn<sub>y</sub>Al<sub>1-y</sub>O<sub>3</sub> outperformed the state-of-the art ceria, producing six times more CO at the same conditions [15]. In addition, La<sub>0.6</sub>Sr<sub>0.4</sub>Cr<sub>0.8</sub>Co<sub>0.2</sub>O<sub>3</sub> had comparable results to ceria though at 300 °C lower temperature [16] and La<sub>0.6</sub>Ca<sub>0.4</sub>Fe<sub>0.4</sub>Mn<sub>0.6</sub>O<sub>3</sub> yielded rates significantly improved compared to ceria [5]. Similarly, selection of elements on the A-and B-sites yielded improved rates for CO<sub>2</sub> conversion and/or lower operation temperatures in the isothermal RWGS-CL process compared to initial results [12, 14]. In these cases, the composition of the perovskite oxide phase was controlled to adjust the redox properties, often quantified in terms of the energy of oxygen vacancy formation [12, 17-19], of the materials under the operation conditions.

There are two primary strategies for tuning the oxygen vacancy formation energy by composition. First, partial substitution of a divalent atom (e.g., Sr) on the normal trivalent A-site forces the transition metal on the B-site to increase its valence charge and/or cause oxygen vacancies to form. Second, population of the B-site with transition metals of various redox abilities dictates the degree of charge balance by its oxidation or formation of oxygen vacancies. As indicated above, these two approaches are often examined simultaneously and more than two metals can be added on each site [20]. Alternatively, in this work, the oxygen vacancy formation energy is tuned by B-site composition through various Fe:Mn:Co ratios while the A-site is fixed with a single element (La). The goals are to determine the effect of composition on the redox properties and evaluate if the B-site doping can compensate for the reducibility lost by eliminating Sr from the A-site. The results indicate it is possible and an isothermal RWGS-CL process can be achieved, similar to previous studies [12, 14] on Sr doped La perovskite oxides. To aid in the evaluation, quantum scale calculations of the electronic structure of the material was conducted to support the microscale experimental results. The combined multiscale investigation of these perovskite oxides elucidates the trail forward to intricate structure-function understanding and design of advanced multifunctional materials of the future.

## 2. Experimental

# 2.1 Material synthesis

LaCo<sub>x</sub>Fe<sub>y</sub>Mn<sub>1-x-y</sub>O<sub>3</sub> perovskites were synthesized using the Pechini Method [21], as done previously [10, 11, 14, 22]. Three samples (Table S1) were synthesized varying

the molar compositions of the metals on the B site, while the A-site was kept as 100% La. The specific formulations are LaCo<sub>0.5</sub>Fe<sub>0.25</sub>Mn<sub>0.25</sub>O<sub>3</sub> (X=0.50 and Y =0.25, named Co50), LaCo<sub>0.25</sub>Fe<sub>0.50</sub>Mn<sub>0.25</sub>O<sub>3</sub> (Y=0.50 and X=0.25, named Fe50), and LaCo<sub>0.25</sub>Fe<sub>0.25</sub>Mn<sub>0.50</sub>O<sub>3</sub> (X=Y=0.25, named Mn50). For each synthesis, an aqueous solution of citric acid (Aldrich, ACS grade ≥99.5%) and stoichiometric amounts, as denoted by the desired composition of the perovskite oxide, of the corresponding precursors La(NO<sub>3</sub>)<sub>3</sub> (Alfa Aesar, 99.9%), Fe(NO<sub>3</sub>)<sub>3</sub> (Aldrich, ≥ 98%), Co(NO<sub>3</sub>)<sub>3</sub> (Acros Organics, 99%), MnCO<sub>3</sub> (Alfa Aesar, 99.9%) were simultaneously stirred and heated to 60 °C for 2 h. Subsequently, ethylene glycol (*grade* ≥99.9; 40 mL) was added. Per literature [23], the ratio of La : B-site : Citric Acid : Ethylene Glycol was 1:1:10:40. For the poly-esterification process, the solution was heated to 90 °C and then stirred for 7 h. The sol-gel was transferred to a crucible and heated to 450 °C for 2 h, with a ramp rate of 20 °C/min. The resulting solid was crushed and calcined at 1200 °C for 6 h.

### 2.2 Material characterization

X-ray powder diffraction (XRD) patterns were collected on a Bruker X-ray diffractometer with Cu K $\alpha$  radiation ( $\lambda$  = 1.54 Å). 2 $\theta$  angles were measured from 20 to 100° at a step size of 0.0102° with collection time per step of 1.2 s. Lattice parameters were calculated by solving the least squares of 2 $\theta$ , using Bragg's Law and the plane spacing equation. X'Pert HighScore Plus software was used to identify the crystal structure and secondary phases. Miller indices (hkl) were obtained from reference patterns. The prominent peak at ~32°, was used to calculate the crystallite size using the Scherrer equation with a shape factor of 0.9.

X-ray photo-electron spectroscopy (XPS) analysis was performed on fresh and post-experiment samples with a Thermo Scientific K-Alpha instrument using Al Kɑ radiation. The pressure in the analysis chamber was on the order of 8e-8 mbar. XPS flood gun supplies Ar ions (99.997%) with a spot size of 400 µm. The pass energy for spectra acquisition was 154.494 eV. The adventitious C1s peak was located at 284.85 eV. Scanning electron microscopy (SEM) was performed with a Hitachi S-800 instrument equipped with an EDAX-Phoenix Energy Dispersive X-Ray Spectrometry (EDS) system. Images were taken with an acceleration voltage of 25 kV.

# 2.3 Temperature-Programmed experiments

An MKS Cirrus Mass Spectrometer (MS) was used to evaluate the reduction and oxidation capabilities of the perovskite oxides. For each experiment, approximately 75 mg of sample was packed in between high-temperature glass wool in a quartz U-tube reactor, positioned inside a furnace. All experiments used He (Airgas, 99.999%) as the carrier gas, 50 sccm of total flow, and, if applicable, the furnace temperature ramp rate was 10 °C/min. All gases were purchased from Airgas in the highest purity available. Alicat mass flow controllers were used to control gas flow. Mass to charge (m/z) of signals 2, 18, 28, and 44 were monitored in the MS corresponding to H<sub>2</sub>, H<sub>2</sub>O, CO, and CO<sub>2</sub>, respectively. For CO quantification, CO<sub>2</sub> fragmentation contribution to m/z = 28 was subtracted.

Temperature programmed reduction (TPR-H<sub>2</sub>) was performed to determine the reduction temperature of the perovskites during the 1<sup>st</sup> step of the RWGS-CL process. 10% H<sub>2</sub> (Airgas, 99.999%)/He was flowed at room temperature, then the sample was heated to 950 °C. Water formed was quantified and correlated to the extent of reduction of the material.

Temperature programmed oxidation (TPO-CO<sub>2</sub>) experiments were performed to identify CO<sub>2</sub> conversion temperature on the reduced perovskites. After reduction of the perovskites at 550 °C under 10% H<sub>2</sub>/He for 30 min, the samples were cooled to room temperature. Then 10% CO<sub>2</sub> (Airgas, 99.999%)/He was flowed until stable. The sample was heated to 950 °C. The amount of CO formed is representative of the CO<sub>2</sub>-conversion capabilities of the reduced materials

## 2.4 Isothermal RWGS-CL

These experiments were largely conducted similarly to the temperature-programmed experiments and used the same reactor system. First, the perovskites were heated under 20% O<sub>2</sub>/He to eliminate the adsorbed CO<sub>2</sub> and, then, were cooled to room temperature. After this, samples were heated to 600 °C, upon signal stabilization, were reduced for 20 min in 10% H<sub>2</sub>/He, flushed for 20 min under He, then 10% CO<sub>2</sub> /He was flowed for 20 min, followed by another 20 min He flushing. This process was repeated four more times for a total of five cycles.

# 2.5 Density Functional Theory Calculations

Density functional theory (DFT) based free energies were computed using the Vienna Ab-initio simulation package (VASP), version 5.3.3 [24-28]. Generalized gradient approximation of the electron densities and Perdew-Burke-Ernzerhof (GGA-PBE)[29] variant of exchange correlation were implemented and the plane wave basis cutoff energy was set to 600 eV. The Brillouin zone of sixty-atom supercell was sampled with a  $4 \times 4 \times 3$  Monkhorst Pack k-point mesh [30]] and the energy computed converged to 1  $\mu$ eV. Different configurations of sixty-atom crystal structure of Co50, Fe50, and Mn50 were tested and the most stable configuration was used for further computations. Bulk oxygen

vacancy formation energy (E<sub>vac</sub>) was calculated following Eq. 1, where  $E_{ABO_3}$  represents the energy of the pure stoichiometric perovskite structure,  $E_{ABO_{3-\delta}}$  is the energy of the oxygen vacant perovskite,  $E_{O_2}$  is the energy of molecular oxygen, n is the number of unit cells, and  $\delta$  is the oxygen vacancy extent. A correction factor of 1.36 eV was applied to  $E_{O_2}$  to account for PBE functional oxygen over-binding error [31].

$$E_{vac} = E_{ABO_{3-\delta}} + \delta \times \frac{n}{2} E_{O_2} - E_{ABO_3}$$
 (1)

 $E_{vac}$  was computed for each active site on the sixty-atom supercell of the three compositions. The optimum  $E_{vac}$  range of 3.36  $\pm$  0.5 eV determined by Maiti et al. was used to evaluate oxygen vacancy and  $CO_2$  conversion capability [12].

Oxidation state of each atom was calculated using the Bader charge analysis algorithm developed by the Henkelman group [32, 33], which integrates the electronic density enclosed in the Bader volume to obtain the charge of an atom. VESTA was used to visualize electron density plots with an isosurface level of 0.0107 e a<sub>0</sub>-3 [34].

## 3. Results and Discussion

Co50, Fe50, and Mn50 samples synthesized via Pechini method achieved an orthorhombic structure (ref# 01-089-2471) (Fig. 1a), which is a main phase found in multiple lanthanum rich perovskites [10, 35]. Markers in Fig. 1b indicated the minor presence of cubic Fe<sub>3</sub>O<sub>4</sub> (ref # 01-085-1436) in Fe50 and Mn50. Presence of Fe<sub>3</sub>O<sub>4</sub> on the XRD patterns could be explained due to excess Fe-precursor on the synthesis or caused by migration of Fe out of the perovskite structure, which would result in a B-site deficient material. EDS elemental mapping of Fe50 sample (Fig. 2) shows all the

elements are well distributed on the bulk structure. Since the Fe50 sample was the best performing one and we used the same synthesis procedure, only one sample was tested for the composition distribution. Co50 and Mn50 have similar morphology to that of Fe50.

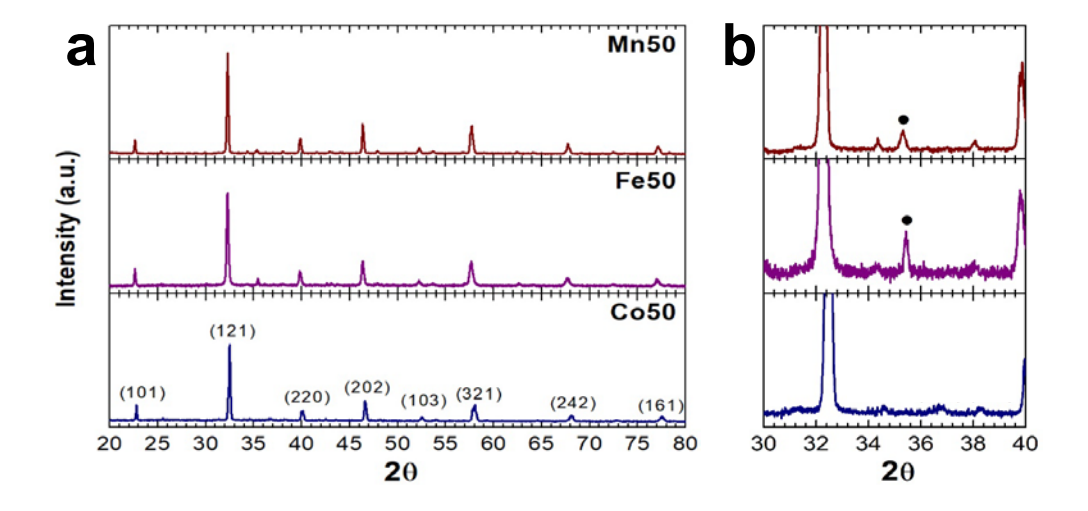


**Figure 1.** X-ray diffraction patterns of as-synthesized Co50, Fe50, and Mn50 samples. (a) Results for full scan and (b) Narrow range indicating Fe<sub>3</sub>O<sub>4</sub> (●) (ref # 01-085-1436) Fe50 and Mn50 samples.

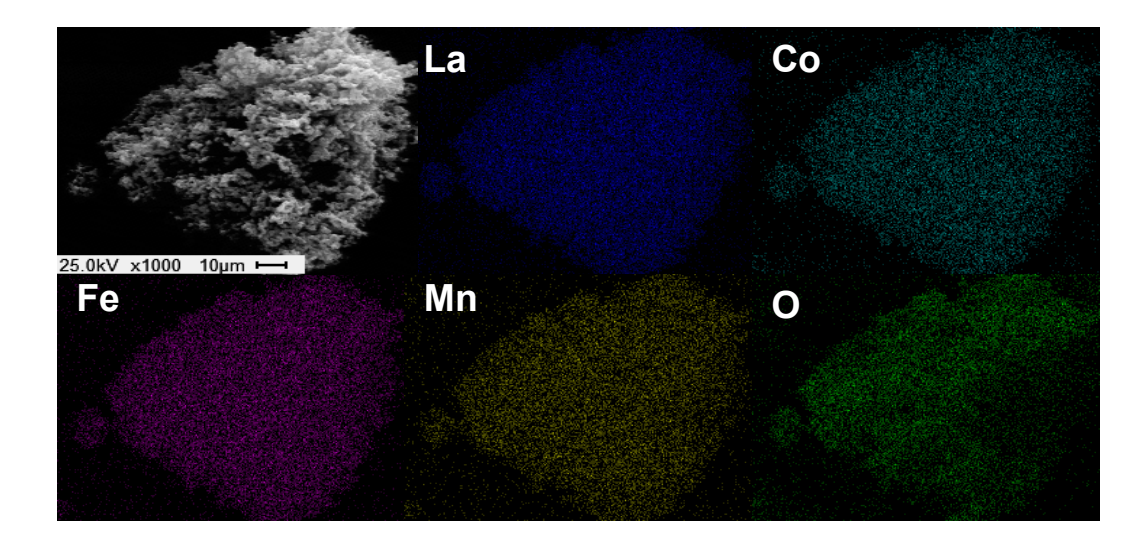
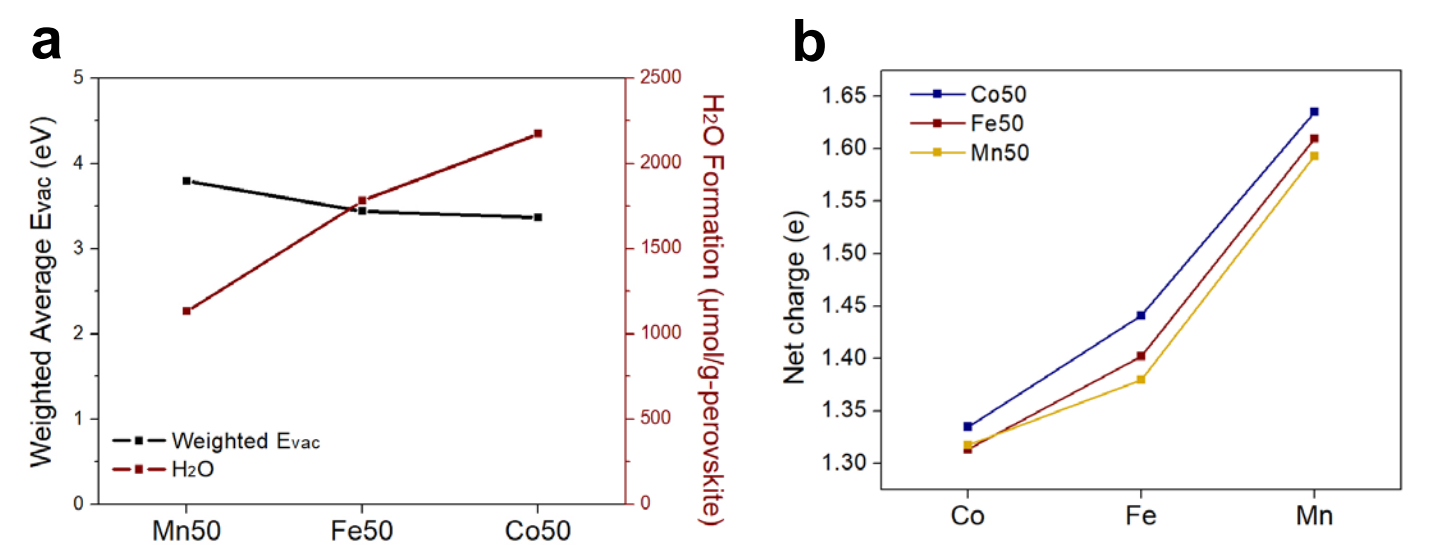


Figure 2. Energy dispersive spectroscopy elemental mapping of Fe50

The introduction of the three metals in the B-site increases the number of sites with different  $E_{\text{vac}}$  values, caused by the presence of multiple valence states and a variety of metal-oxygen bonds. Oxidation states of the transition metals (as obtained through Bader calculation) exhibit charge variation within the structure, thereby creating metal-oxygen bonds of varying strengths. Similarly, doping of  $Sr^{2+}$  in a LaMnO<sub>3</sub> perovskite has been reported to introduce a mixture  $Mn^{3+}$  and  $Mn^{4+}$  states, where  $Mn^{3+}$ -O bonds have different ionic strength than  $Mn^{4+}$ -O bonds [15, 17, 36]. Site-weighted average oxygen vacancy formation energy ( $E_{\text{vac}}$ ) is thus an appropriate descriptor of the vacancy formation characteristics of these perovskite oxides. The  $E_{\text{vac}}$  values (Fig. 3a) calculated for all three perovskite compositions (Co50, Fe50, Mn50) fall within the optimum range of 3.36  $\pm$  0.5 eV [12] predicting high oxygen vacancy formation and  $CO_2$  conversion capabilities. The theoretical trend of  $E_{\text{vac}}$  matches with the experimental water formation (indicating oxygen vacancy formation).



**Figure 3.** (a) DFT-calculated E<sub>vac</sub> results correlated to experimental amount of oxygen vacancies formed. (b) Average net charge on each transition metal

The net charge (Fig. 3b) for Co50 is higher for each constituent transition metal than for Fe50 and Mn50, indicating higher charge localization than the Fe50 and Mn50 structures. This distribution of charge can be visualized in Fig. S1, where Mn50 and Fe50 exhibit slightly higher electron density between M-O bonds than Co50. The increased electron density exhibited in the interatomic regions are representative of stronger bonds that require higher energy for oxygen removal.

In general, temperature programmed reduction experiments of perovskite oxides exhibit two reduction areas, the lowest temperature peak is representative of oxygen vacancy formation on the oxides, whereas the highest temperature one, corresponds to the decomposition of the oxygen vacant perovskites to its base oxides. TPR-H2 experiments (Fig. 4a) show Co50 starts reducing at 270 °C, whereas Fe50 and Mn50 start forming vacancies at 400 °C, indicating that the Co-rich perovskite (Co50) is more easily reducible than the other two samples, agreeing with the theoretical trends of Co50 exhibiting lower E<sub>vac</sub> than Fe50 and Mn50 (Fig. 3a), and several other computational studies predicting easier oxygen vacancy formation over Co-rich oxides [12]. This favorable reduction of Co also causes Co50 to start decomposing to base oxides at ~ 100 °C earlier than Fe50 and Mn50 (second peak in the TPR-H<sub>2</sub> profiles). Mn50 seems to have an additional transition in the low-temperature area, likely due to Mn undergoing more oxidation states transitions than Fe or Co. At ~550 °C, all the samples have undergone the formation of oxygen vacancies (passed the low-temperature reduction area) but have not transitioned to the base oxides (before the high-temperature reduction area). Therefore, this temperature was chosen as the reduction temperature for the subsequent oxidation (TPO-CO<sub>2</sub>) experiment. Choosing a temperature below the high

temperature reduction area would contribute to keeping the material in a single crystalline phase when undergoing RWGL-CL cycles.

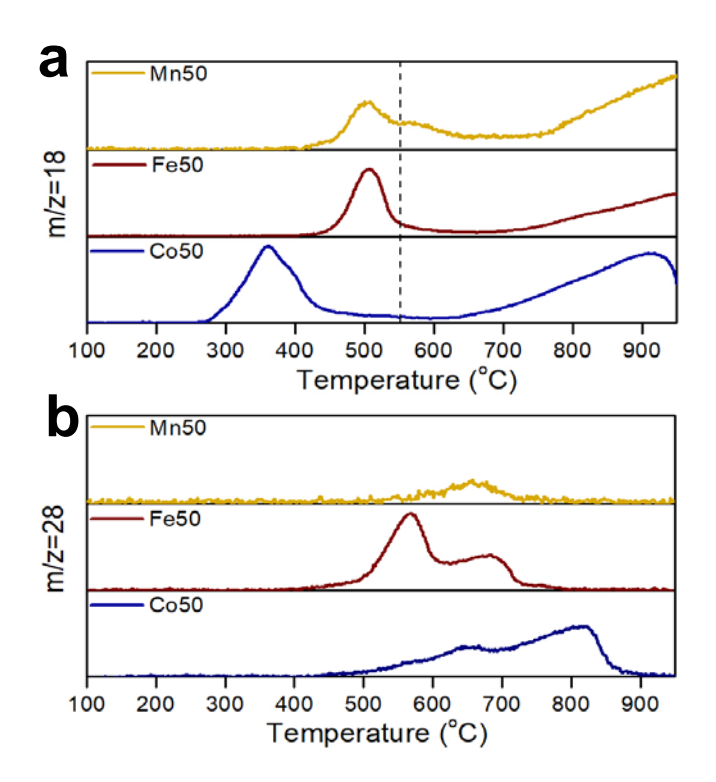


**Figure 4.** TPR-H<sub>2</sub> and TPO-CO<sub>2</sub> profiles. (a) TPR-H<sub>2</sub>: water formation as a mark of oxygen vacancy formation (m/z=18 signal) for different reaction temperatures. The dotted line represents the reduction temperature chosen for TPO-CO<sub>2</sub> experiment (b) TPO-CO<sub>2</sub>: CO formation (m/z=28 signal) as a function of reaction temperatures.

Integrating the area under the curve in Figure 4.b (Table 1) reveals that Co50 converted more CO<sub>2</sub> to CO than Mn50, Fe50 and a reference material La<sub>0.75</sub>Sr<sub>0.25</sub>FeO<sub>3</sub> (LSF) [14]. Both Fe50 and Co50 exhibit two CO<sub>2</sub> conversion regions. Similar Co-based perovskites have shown two or more re-oxidation areas after their reduction, suggesting the reduced perovskite underwent several phase transitions during their re-oxidation with CO<sub>2</sub>, these result is in agreement with the profiles of reduced oxides in Figure 6, or could also be a consequence of the changes of oxidation state of the metals on the B-site of

the perovskite, suggesting that co-existence of certain combinations of oxidation states of the metals on the B-site are more favored to re-oxidize than others. The onset CO<sub>2</sub>-conversion temperature between Co50 and Fe50 was similar (and lower than Mn50), which indicates the reduced state of Mn50 is less favored to re-oxidize with CO<sub>2</sub> as the other samples. It is to be noted that Fe50 produces more CO at lower temperatures (below 600 °C) than Co50, which makes Fe50 appealing for its possibility of demonstrating an isothermal RWGS-CL cycle. The reduction profiles in Figure 4a and the 200 °C difference in the peak CO formation temperatures between Co50 and Fe50 in figure 4b, suggest that Co50 is more favored to reduce at low temperatures but less favored to re-oxidize with CO<sub>2</sub> when compared to and Fe50.

Fe50, on the other hand, converted 1420 µmol CO/g-perovskite at a peak temperature of 570 °C. The onset decomposition temperature is higher at 700 °C, making an isothermal RWGS-CL process feasible. These results agree with our previous study with LaSrFe perovskites, indicating that the redox abilities of the material are highly dependent on the predominant B-site metal.

**Table 1.** Water formation (oxygen vacancy generation) and CO in µmol/g-perovskite calculated from integrating the area under the curve from Fig. 4a and 4b, respectively, and peak CO<sub>2</sub> conversion temperature.

Sample Name	H <sub>2</sub> O formation (μmol/g- perovskite)	CO formation (µmol/g-perovskite)	Peak Oxidation Temperature (°C)
Mn50	1130	390	660
Fe50	1790	1420	570
Co50	2170	1780	815

Upon reduction, Co50 and Mn50 formed small amounts of metallic Co and Mn respectively (Fig. 5), as seen previously likely due to the high reducibility of Co and the multiple oxidation states Mn can attain. Metallic Mn was also noted on the reduced Fe50. These reduced metals, were not seen on the XRD profiles of the materials after oxidation with CO<sub>2</sub>, indicating that upon reduction, a small amount of B-site metals migrated out of the original perovskite structured, and re-incorporated back into the structure after re-oxidation with CO<sub>2</sub>. Similarly, Fe<sub>3</sub>O<sub>4</sub> disappears from the XRD on the reduced Fe50, and reappears on the XRD profile after CO<sub>2</sub> conversion.

For all the materials, the XRD-profiles shifted to lower 2-theta values indicating an increase in lattice parameters due to their reduction and thermal expansion. In previous studies, it has been shown that reducing  $La_{1-Y}Sr_{Y}CoO_{3}$  perovskites into their high-temperature reduction area, can lead to sufficient Co migrating out of the perovskite structure, thus causing its decomposition into a Ruddlesden-Popper perovskite ( $La_{2-Y}Sr_{Y}CoO_{4}$ ) and metallic Co [10], noticeable by a diffraction line at ~32  $20^{\circ}$  (1  $20^{\circ}$  lower than the main perovskite line at 33  $20^{\circ}$ ). In this study, none of the samples exhibits a Ruddlesden-Popper diffraction line at ~32  $20^{\circ}$ , which shows the original perovskite phase was maintained in all cases. Nonetheless, though minor, the presence of small amounts of metallic Co, were enough to cause different re-oxidation profiles on the reduced samples, as seen in Figure 4b.

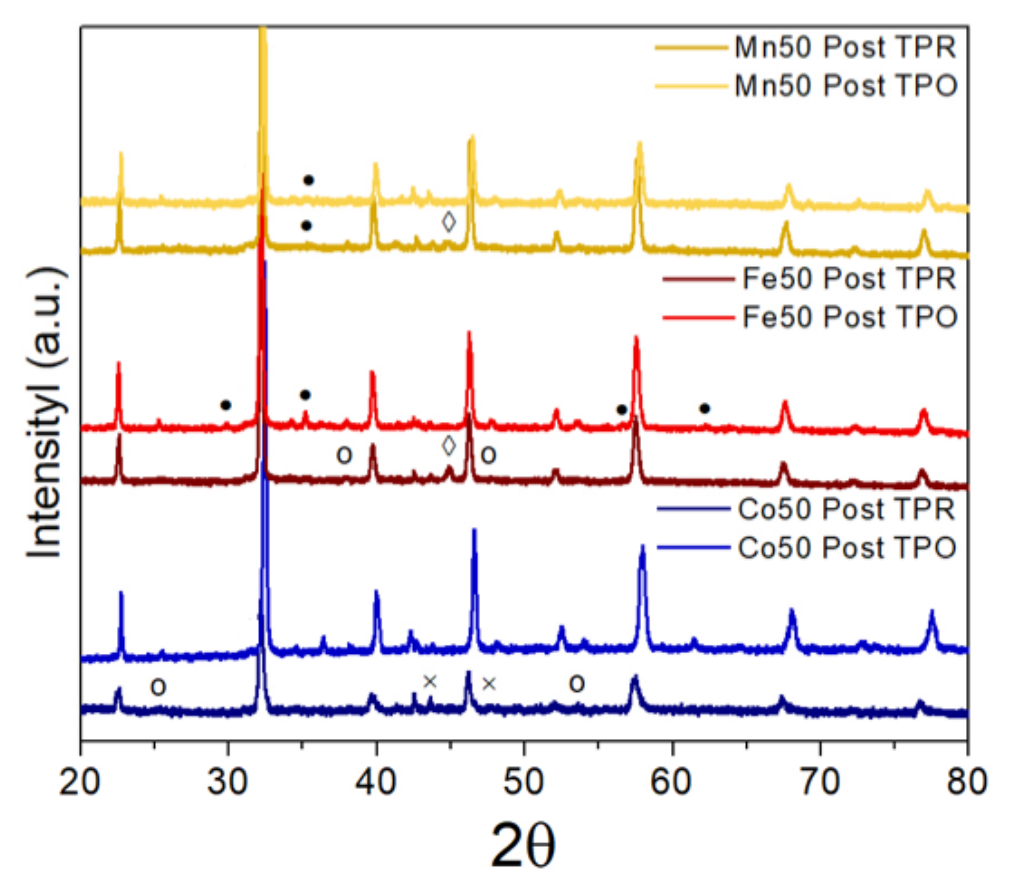


**Figure 5**. X-ray diffraction pattern for Co50, Fe50, and Mn50 after TPR-H<sub>2</sub> and TPO-CO<sub>2</sub>. For each pair, the post reduction profile is on the bottom, and post TPO-CO<sub>2</sub> on the top. Other observed phases include: Mn ( $\Diamond$ ), Co ( $\times$ ) and Fe<sub>3</sub>O<sub>4</sub> ( $\bullet$ ).

Crystallite size after TPR (Table 2) is lower for Co50 followed by Fe50 and Mn50, the same trend as  $CO_2$  generation, suggesting lower crystallite size after reduction enhances  $CO_2$  conversion. After oxidation, Mn50's crystallite size increased by 60%. This increase in crystallite size during the oxidation step hindered the reaction, generating only 390  $\mu$ mol CO/g-perovskite.

Table 2. Volume and crystallite size calculated from XRD

Sample Name	V <sup>a</sup> fresh (Å <sup>3</sup> )	<b>V</b> <sup>a</sup> роsт-тро (Å <sup>3</sup> )	L <sup>b</sup> FRESH (Å)	L <sup>b</sup> POST-TPR (Å)	L <sup>b</sup> POST-TPO (Å)	
Mn50	239	238	489	365	765	
Fe50	239	241	356	308	373	
Co50	236	237	418	243	372	

<sup>&</sup>lt;sup>a</sup> V represents cell volume; <sup>b</sup> L represents crystallite size

XPS analysis on fresh and post-TPO samples display the change in valence state after oxidation and the possible effects after multiple cycles. La  $3d_{5/2}$  and La  $3d_{3/2}$  peaks (Fig. S2) binding energy correspond to 833.7 eV and 838 eV, representative of La<sub>2</sub>O<sub>3</sub> peaks [37]. The difference between  $3d_{5/2}$  multiplet peaks (~4.3 eV) confirms the trivalent state [38]. All the post-TPO samples showed shifts to lower binding energies that marks mild reduction of lanthanum oxidation states due to oxygen vacancy formation.

Figure 6a. shows the Co-2p x-ray photoelectron spectra. Since both Co-2p<sub>3/2</sub> and Co-2p<sub>1/2</sub> exhibit similar B.E. for CoO and Co<sub>3</sub>O<sub>4</sub> [39], the oxidation states for Co are identified mainly by the position of Co-2p satellite features. Co<sub>5</sub>O samples have more pronounced satellite features due to the presence higher Co content in the sample. Close observation suggests post TPO Co<sub>5</sub>O sample has more Co(+2) states as the satellite peak (~805 eV) shifts to the lower binding energies (B.E.). The Co-2p<sub>1/2</sub> satellite peak for Fe<sub>5</sub>O and Mn<sub>5</sub>O are also shifted to the lower B.E. than that of Co<sub>5</sub>O, thereby revealing lower oxidation states of Co ions in Fe and Mn rich samples. This is also predicted from the DFT-calculated results (Fig. 3b) where we observe the same trend of lower Co oxidation states for Fe<sub>5</sub>O and Mn<sub>5</sub>O samples.

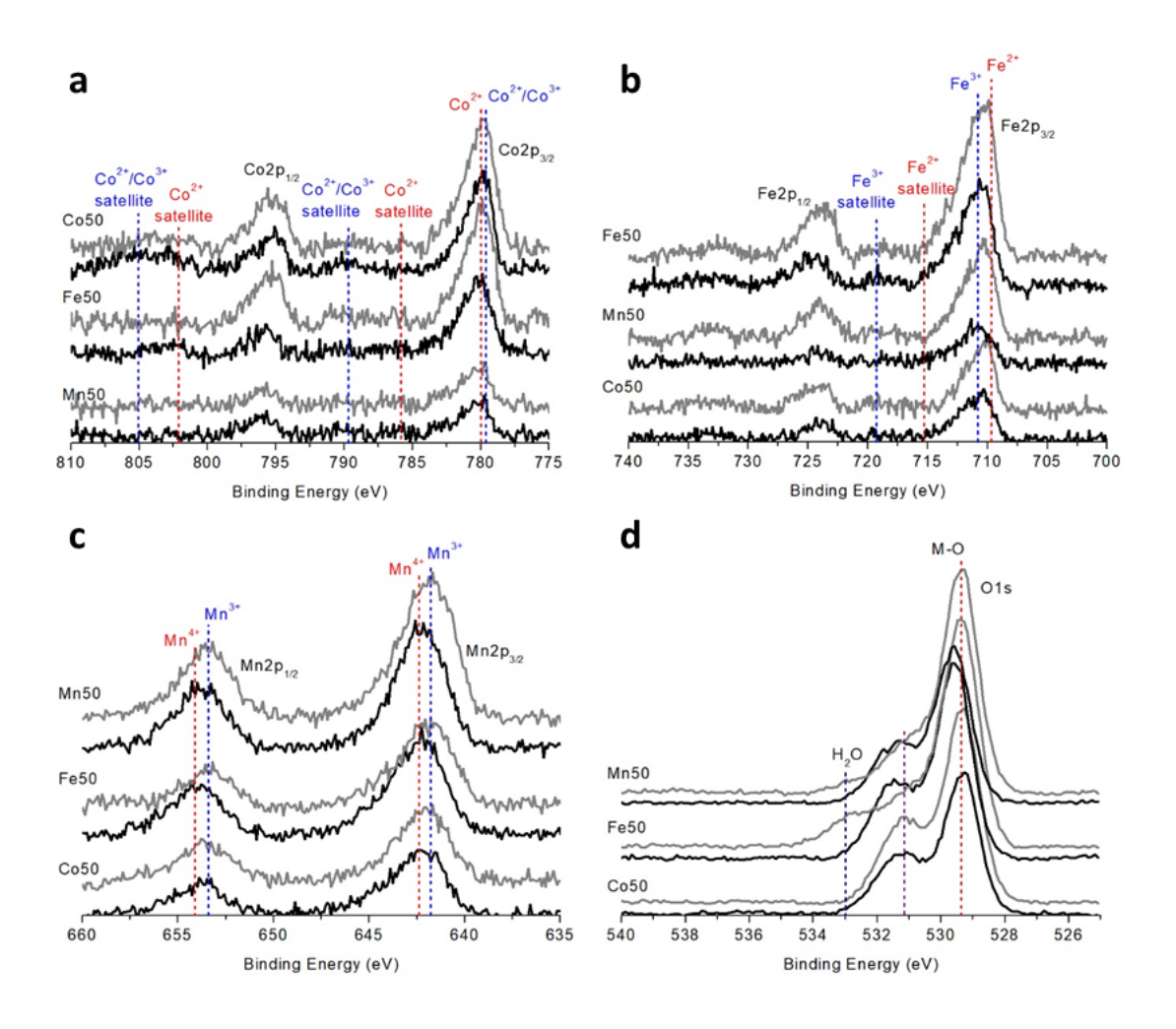


**Figure 6.** X-ray photo-electron spectra (a) Co-2p, (b) Fe-2p, (c) Mn-2p, and (d) O-1s for fresh (black) and post-TPO (grey) samples.

Fe-2p<sub>3/2</sub> peak and satellites features for FeO and Fe<sub>2</sub>O<sub>3</sub> are used to identify oxidation states. The bump that ranges from 715 eV to 720 eV (Fig. 6b) is indicative of Fe<sup>2+</sup> (715.4 eV) and Fe<sup>3+</sup> (719.3 eV) [39]. After TPO, the main 2p<sub>3/2</sub> peak shifts to lower binding energy for all materials, indicating Fe<sup>2+</sup> becomes predominant after regeneration. This reduction of metal ions after TPO is attributed to mild presence of oxygen vacancies after TPO [14], thus resulting in decreased oxidation states of the metal ions. The broad peaks for both Mn-2p<sub>3/2</sub> and Mn-2p<sub>1/2</sub> peaks (Fig. 6c) indicate there is presence of mixed valence states Mn<sup>3+</sup>/Mn<sup>4+</sup>. 2p<sub>3/2</sub> peaks positioned at 641.8 eV and 642.4 eV are assigned

to Mn<sup>3+</sup> and Mn<sup>4+</sup> respectively [39]. After CO<sub>2</sub> conversion, peaks shift towards lower binding energy indicating Mn<sup>3+</sup> predominance over Mn<sup>4+</sup>.

O-1s spectra for the perovskite oxides depicts a major O1s peak (around ~529.5 eV) corresponding to M-O bonds [38, 40]. The post TPO samples show a shift of this peak towards lower B.E. This is attributed to minor reduction of the oxidation states of the metals as observed for Co-2p, Mn-2p and Fe-2p spectra as well (Figs. 6a-c). The peak around 531 eV marks the presence of carbonate [40] as also observed around 289 eV of C-1s spectra (Fig. S4). The minor peak around 533 eV can be due to the presence of surface adsorbed water as well as oxygen vacancies [40, 41]. The increased intensity for post TPO samples justifies the presence of both as increased oxygen vacancies are more probable after RWGS-CL experiments and oxygen deficient surfaces are more prone to adsorb moisture.

As shown in Table 3, the Co/La, Fe/La, and Mn/La atomic ratios, for as synthesized and post-TPO samples are compared in terms of the near surface (XPS) and near bulk (EDS) techniques. Fresh surface atomic ratios for Co50 and Mn50 show the surface composition obtained from XPS are similar to the bulk composition obtained from EDS. For Fe50, cobalt is promoted to the surface to almost the same ratio. This means similar amounts of Co-O and Fe-O bonds are available on the surface, allowing Fe50 to create similar amount of oxygen vacancies as Co50. Co50 creates more oxygen vacancies because it has more Co-O bonds available on the surface which are easier to break than Fe-O and Mn-O.

**Table 3.** Atomic ratio of Co50, Fe50, Mn50 fresh Co-2p, Fe-2p, Mn-2p and La-3d XPS and EDS.

	XPS			EDS		
	Co/La	Fe/La	Mn/La	Co/La	Fe/La	Mn/La
Co50 fresh	0.64	0.41	0.30	0.56	0.26	0.21
Co50 post TPO	0.58	0.51	0.27	-	-	-
Fe50 fresh	0.64	0.67	0.42	0.44	0.78	0.31
Fe50 post TPO	0.90	1.23	0.45	-	-	-
Fe50 5 cycles	0.84	1.32	0.39	-	-	-
Mn50 fresh	0.26	0.35	0.69	0.33	0.31	0.51
Mn50 post TPO	0.12	0.73	0.66	-	-	-

The stability of Fe50 was tested over five isothermal RWGS-CL cycles (Fig. 7) at  $600\,^{\circ}$ C. Consistent to previous results [11, 14], oxygen atoms removed from the sample in the first reduction includes adsorbed oxygen which is linked to the pre-treatment in conditions simulated air ( $20\%\,O_2/He$ ). After the  $1^{st}$  cycle,  $H_2O$  formation per cycle significantly decreases to ~1200 umol of  $H_2O/g$  perovskite, and remains relatively constant (between 1100 and 1200 umol  $H_2O/g$  perovskite, corresponding to ~0.27 mol  $H_2O/g$  mol perovskite) after the final cycle.

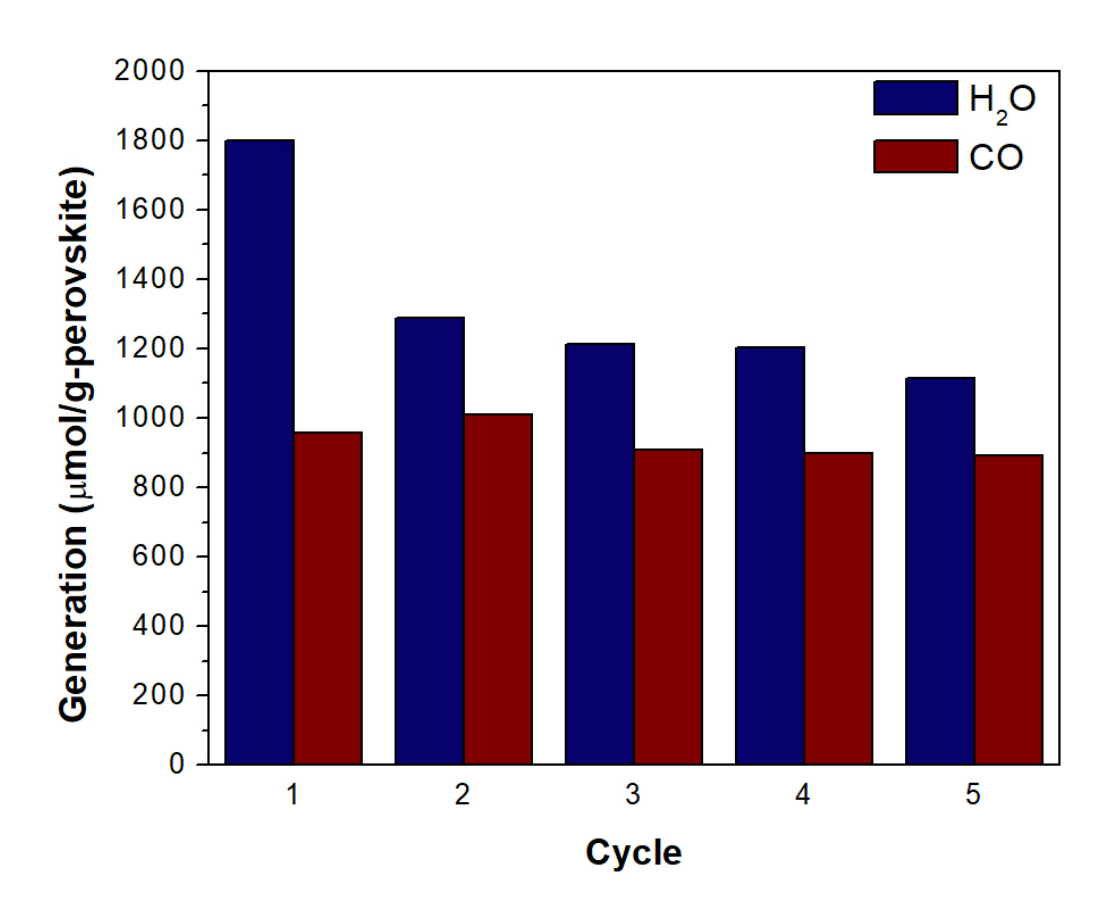


**Figure 7.** Five cycle experiment on Fe50 showing water (oxygen vacancies) and carbon monoxide generation in µmol/g-perovskite.

Reaching a stable formation of CO throughout the cycles (~ 900 umol CO/g perovskite, corresponding to ~ 0.22 mol CO/mol perovskite) suggests that the formation of CO is limited by the amount of oxygen vacancies the material is able to form at the reducing conditions, but maximized in this particular oxide. Earlier studies showed that the amount of oxygen vacancies forming decreased slightly with each cycle, gradually approaching the amount of CO generated [14]. This trend suggested oxygen vacancies formed initially were not sufficiently regenerated on the initial cycles and oxygen shuttling occurred at substoichiometric levels. In this case, oxygen shuttling occurred from ~ delta values from ~2.6 to 2.8 during the final cycles. Since CO<sub>2</sub> is a weaker oxidizing agent

than H<sub>2</sub> is a reducing agent at this conditions for this material, the cycling occurred at substoichiometric amounts of oxygen. Oxygen shuttling at substoichiometric oxygen amounts suppresses reduction since the sample is partially reduced at the beginning of the reduction step after a couple cycles. Maintaining similar oxygen vacancy formation and CO generation (as exhibited by Fe50 on Figure 7) is important to avoid decomposition of the material [14] without periodically (or at least less frequently) oxidizing the material with a stronger oxidizing agent such as air to regenerate the perovskite oxide structure. This material maintained its crystalline structure as observed by XRD (Fig. S3) and SEM (Fig. 8) indicated the lack of morphology change for Fe50 after five RWGS-CL cycles. Multiple valence states were present after TPO, as observed by XPS (Fig. 6), which allows for stable CO generation. Due to this behavior, and due to Fe50 being among the highest performance materials yielding 900 μmol CO/g-perovskite, Fe50 is a promising material for CO<sub>2</sub> conversion by thermochemical methods.

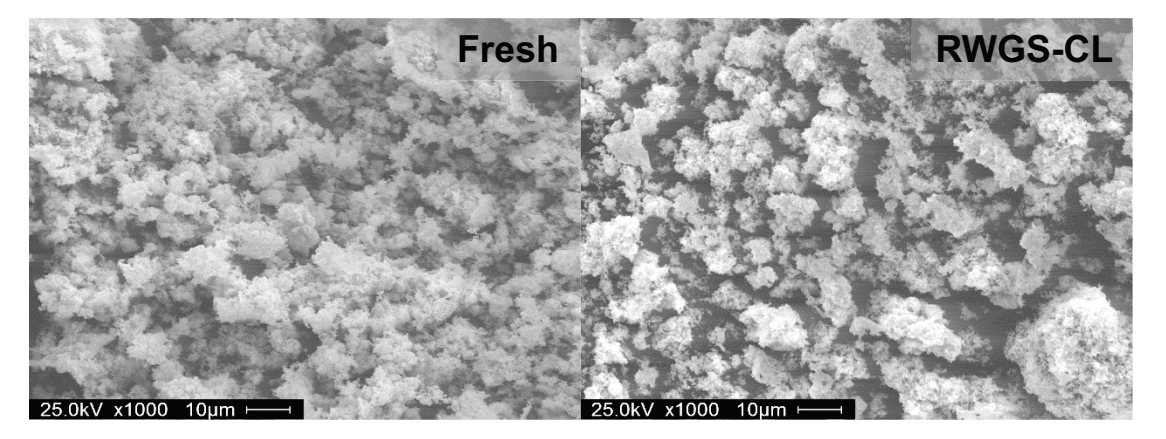


**Figure 8.** Scanning electron microscopy of Fe50 before and after isothermal RWGS-CL cycles

#### 4. Conclusion

The simultaneous doping of three transition metals (Co, Fe, and Mn) in the B-site of the perovskite oxide structure was studied computationally and experimentally. Density functional theory-based calculations depict the reluctance of the Mn rich sample (Mn50) to exhibit oxygen vacancies. The Co rich sample (Co50), although promoting easy oxygen vacancy formation, was conducive to decomposition under RWGS-CL operation. In contrast, the higher Fe composition induced reduction and oxidation at similar temperatures, making it an ideal candidate material for isothermal RWGS-CL process. Isothermal RWGS-CL cycles at 600 °C revealed Fe50 is capable of steady CO generation without decomposition. Experimental results reveal multiple valence states on the surface, enhancing CO<sub>2</sub> conversion further than reported materials with two cations. Higher CO<sub>2</sub> conversion was achieved over oxygen deficient samples with smaller crystallite size (higher exposed surface are for CO2 conversion reactions). This was observed with Mn50, where the crystallite size increased during oxidation and resulted in lower CO<sub>2</sub> conversion than expected, while the decreased Co<sub>5</sub>0 crystallite size enhanced its CO<sub>2</sub> conversion performance.

## Acknowledgements

This study was funded by National Science Foundation through CBET-1335817, IIP-1743623, and CHE-1531590 grants. Authors would also like to acknowledge funding from the Venturewell E-Team and NASA through the Florida Space Grant Consortium. Y.A.D. acknowledges the Florida Education Fund for the McKnight Dissertation Fellowship.

Additional thanks goes to research computing at USF for computational resources, Yajing

Chang for SEM and EDS, and Dr. Anne J. Meier for XPS measurements.

## References

- [1] T. Maverick, A Carbon Capture and Storage Breakthrough, Wall St. Daily, last accessed 8/19/2016 (2014).
- [2] Y.A. Daza, J.N. Kuhn, CO<sub>2</sub> conversion by reverse water gas shift catalysis: Comparison of catalysts, mechanisms and their consequences for CO<sub>2</sub> conversion to liquid fuels, RSC Advances, 6 (2016) 49675-49691.
- [3] G.A. Olah, The Role of Catalysis in Replacing Oil by Renewable Methanol Using Carbon dioxide Capture and Recycling (CCR), Catalysis Letters, 143 (2013) 983.
- [4] D.S. Mallapragada, N.R. Singh, V. Curteanu, R. Agrawal, Sun-to-Fuel Assessment of Routes for Fixing CO<sub>2</sub> as Liquid Fuel, Industrial & Engineering Chemistry Research, 52 (2013) 5136–5144.
- [5] W.C. Chueh, C. Falter, M. Abbott, D. Scipio, P. Furler, S.M. Haile, A. Steinfeld, High-Flux Solar-Driven Thermochemical Dissociation of CO<sub>2</sub> and H<sub>2</sub>O Using Nonstoichiometric Ceria, Science, 330 (2010) 1797-1801.
- [6] J.R. Scheffe, D. Weibel, A. Steinfeld, Lanthanum-Strontium-Manganese Perovskites as Redox Materials for Solar Thermochemical Splitting of H<sub>2</sub>O and CO<sub>2</sub>, Energy & Fuels, 27 (2013) 4250-4257.
- [7] P. Furler, J.R. Scheffe, A. Steinfeld, Syngas production by simultaneous spliting of H<sub>2</sub>O and CO<sub>2</sub> via ceria redox reactions in a high-temperature solar reactor, Energy & Environmental Science, 5 (2012) 6098-6103.
- [8] V.V. Galvita, H. Poelman, V. Bliznuk, C. Detavernier, G.B. Marin, CeO<sub>2</sub>-Modified Fe2O3 for CO2 Utilization via Chemical Looping, Ind. Eng. Chem. Res., 52 (2013) 8416–8426.
- [9] N.V.R.A. Dharanipragada, L.C. Buelens, H. Buelens, E. De Grave, V.V. Galvita, G.B. Marin, Mg–Fe–Al–O for advanced CO<sub>2</sub> to CO conversion: carbon monoxide yield vs. oxygen storage capacity, Journal of Mater. Chem. A, 3 (2015) 16251–16262.
- [10] Y.A. Daza, R.A. Kent, M.M. Yung, J.N. Kuhn, Carbon Dioxide Conversion by Reverse Water–Gas Shift Chemical Looping on Perovskite-Type Oxides, Industrial & Engineering Chemistry Research, 53 (2014) 5828–5837.
- [11] B.J. Hare, D. Maiti, Y.A. Daza, V.R. Bhethanabotla, J.N. Kuhn, Enhanced CO<sub>2</sub> Conversion to CO by Silica-Supported Perovskite Oxides at Low Temperatures, ACS Catalysis, 8 (2018) 3021-3029.
- [12] D. Maiti, B.J. Hare, Y.A. Daza, A.E. Ramos, J.N. Kuhn, V.R. Bhethanabotla, Earth Abundant Perovskite Oxides for Low Temperature Thermochemical CO<sub>2</sub> Conversion, Energy & Environmental Science, 11 (2018) 648-659.
- [13] M. Wenzel, L. Rihko-Strukmann, K. Sundmacher, Thermodynamic Analysis and Optimization of RWGS Processes for Solar Syngas Production from CO<sub>2</sub>, AICHE Journal, 63 (2016) 15-22.

- [14] Y.A. Daza, D. Maiti, R.A. Kent, V.R. Bhethanabotla, J.N. Kuhn, Isothermal reverse water gas shift chemical looping on La<sub>0.75</sub>Sr<sub>0.25</sub>Co<sub>(1-Y)</sub>Fe<sub>Y</sub>O<sub>3</sub> perovskite-type oxides, Catal. Tod., 258 (2015) 691-698.
- [15] A.H. McDaniel, E.C. Miller, D. Arifin, A. Ambrosini, E.N. Coker, R. O'Hayre, W.C. Chueh, J. Tong, Sr- and Mn-doped LaAlO<sub>3-δ</sub> for solar thermochemical H<sub>2</sub> and CO production, Energy & Environmental Science, 6 (2013) 2024-2028.
- [16] A.H. Bork, M. Kubicek, M. Struzik, J.L.M. Rupp, Perovskite La<sub>0.6</sub>Sr<sub>0.4</sub>Cr<sub>1-x</sub>Co<sub>x</sub>O<sub>3-δ</sub> solid solutions for solar-thermochemical fuel production: strategies to lower the operation temperature, Journal of Materials Chemistry A, 3 (2015) 15546-15557.
- [17] A.M. Deml, V. Stevanović, A.M. Holder, M. Sanders, R. O'Hayre, C.B. Musgrave, Tunable Oxygen Vacancy Formation Energetics in the Complex Perovskite Oxide Sr<sub>x</sub>La<sub>1-x</sub>Mn<sub>y</sub>Al<sub>1-y</sub>O<sub>3</sub>, Chemistry of Materials, 26 (2014) 6595-6602.
- [18] A.M. Deml, V. Stevanović, C.L. Muhich, C.B. Musgrave, R. O'Hayre, Oxide enthalpy of formation and band gap energy as accurate descriptors of oxygen vacancy formation energetics, Energy & Environmental Science, 7 (2014) 1996-2004.
- [19] D. Maiti, Y.A. Daza, M.M. Yung, J.N. Kuhn, V.R. Bhethanabotla, Oxygen vacancy formation characteristics in the bulk and across different surface terminations of  $La_{(1-x)}Sr_xFe_{(1-y)}Co_yO_{(3-\delta)}$  perovskite oxides for  $CO_2$  conversion, Journal of Materials Chemistry A, 4 (2016) 5137-5148.
- [20] N. Lakshminarayanan, H. Choi, J.N. Kuhn, U.S. Ozkan, Effect of additional B-site transition metal doping on oxygen transport and activation characteristics in La<sub>0.6</sub>Sr<sub>0.4</sub>(Co<sub>0.18</sub>Fe<sub>0.72</sub>X<sub>0.1</sub>)O<sub>3-1</sub> (where X= Zn, Ni or Cu) perovskite oxides, Applied Catalysis B: Environmental, 103 (2011) 318–325.
- [21] M. Popa, M. Kakihana, Synthesis of lanthanum cobaltite (LaCoO<sub>3</sub>) by the polymerizable complex route, Solid State Ionics, 151 (2002) 251-257.
- [22] B.J. Hare, D. Maiti, S. Ramani, A.E. Ramos, V.R. Bhethanabotla, J.N. Kuhn, Thermochemical conversion of carbon dioxide by reverse water-gas shift chemical looping using supported perovskite oxides, Catalysis Today, 323 (2019) 225-232.
- [23] S. Ivanova, A. Senysshyn, E. Zhecheva, K. Tenchev, V. Nikolov, R. Stoyanova, H. Fuess, Effect of the synthesis route on the microstructure and the reducibility of LaCoO<sub>3</sub>, Journal of Alloys and Compounds, 480 (2009) 279-285.
- [24] P. Hohenberg, W. Kohn, Inhomogeneous Electron Gas, Physical Review, 136 (1964) B864-B871.
- [25] W. Kohn, L.J. Sham, Self-Consistent Equations Including Exchange and Correlation Effects, Physical Review, 140 (1965) A1133-A1138.
- [26] G. Kresse, J. Furthmüller, Efficient iterative schemes for *ab initio* total-energy calculations using a plane-wave basis set, Physical Review B, 54 (1996) 11169-11186.
- [27] G. Kresse, J. Furthmüller, Efficiency of ab-initio total energy calculations for metals and semiconductors using a plane-wave basis set, Computational Materials Science, 6 (1996) 15-50.
- [28] G. Kresse, J. Hafner, *Ab initio* molecular dynamics for liquid metals, Physical Review B, 47 (1993) 558-561.
- [29] J.P. Perdew, K. Burke, M. Ernzerhof, Generalized Gradient Approximation Made Simple, Physical Review Letters, 77 (1996) 3865-3868.
- [30] H.J. Monkhorst, J.D. Pack, Special points for Brillouin-zone integrations, Physical Review B, 13 (1976) 5188-5192.

- [31] L. Wang, T. Maxisch, G. Ceder, Oxidation energies of transition metal oxides within the GGA + U framework, Physical Review B, 73 (2006) 195107 (195101-195106). [32] W. Tang, E. Sanville, G. Henkelman, A grid-based Bader analysis algorithm without lattice bias, J Phys Condens Matter, 21 (2009) 084204-084201 084204-084207. [33] G. Henkelman, A. Arnaldsson, H. Jónsson, A fast and robust algorithm for Bader decomposition of charge density, Computational Materials Science, 36 (2006) 354-360. [34] K. Momma, F. Izumi, VESTA 3 for three-dimensional visualization of crystal, volumetric and morphology data, Journal of Applied Crystallography, 44 (2011) 1272-1276.
- [35] Q. Jiang, J. Tong, G. Zhou, Z. Jiang, Z. Li, C. Li, Thermochemical CO<sub>2</sub> splitting reaction with supported La<sub>x</sub>A<sub>1-x</sub>Fe<sub>y</sub>B<sub>1-y</sub>O<sub>3</sub> (A=Sr, Ce, B=Co, Mn;  $0 \le x$ , y≤1) perovskite oxides, Solar Energy, 103 (2014) 425-437.
- [36] A. Demont, S. Abanades, E. Beche, Investigation of Perovskite Structures as Oxygen-Exchange Redox Materials for Hydrogen Production from Thermochemical Two-Step Water-Splitting Cycles, The Journal of Physical Chemistry C, 118 (2014) 12682-12692.
- [37] M. O'Connell, A.K. Norman, C.F. Hutteramnn, M.A. Morris, Catalytic oxidation of lanthanum-transition metal perovskite materials, Catalysis Today, 47 (1999) 123. [38] H.S. Fogler, Elements of Chemical Reaction Engineering 4th ed. ed., Pearson, New York, 2006.
- [39] M.C. Biesinger, B.P. Payne, A.P. Grosvenor, L.W.M. Lau, A.R. Gerson, R.S.C. Smart, Resolving surface chemical states in XPS analysis of first row transition metals, oxides and hydroxides: Cr, Mn, Fe, Co and Ni, Applied Surface Science, 257 (2011) 2717-2730.
- [40] N.A. Merino, B.P. Barbero, P. Eloy, L.E. Cadús, La<sub>1-x</sub>Ca<sub>x</sub>CoO<sub>3</sub> perovskite-type oxides: Identification of the surface oxygen species by XPS, Applied Surface Science, 253 (2006) 1489-1493.
- [41] S. Jaiswar, K.D. Mandal, Evidence of Enhanced Oxygen Vacancy Defects Inducing Ferromagnetism in Multiferroic CaMn<sub>7</sub>O<sub>12</sub> Manganite with Sintering Time, The Journal of Physical Chemistry C, 121 (2017) 19586-19601.